



AFRL-RQ-WP-TP-2014-0133

THIN FILM EVAPORATION MODEL WITH RETARDED VAN DER WAALS INTERACTION (POSTPRINT)

Michael Hanchak, Marlin D. Vangsness, and Jamie S. Ervin

University of Dayton Research Institute

Nadina Gheorghiu

Universal Technology Corporation

Larry Byrd and John G. Jones

**Mechanical and Thermal Systems Branch
Power and Control Division**

NOVEMBER 2013

Approved for public release; distribution unlimited.

See additional restrictions described on inside pages

STINFO COPY

**AIR FORCE RESEARCH LABORATORY
AEROSPACE SYSTEMS DIRECTORATE
WRIGHT-PATTERSON AIR FORCE BASE, OH 45433-7542
AIR FORCE MATERIEL COMMAND
UNITED STATES AIR FORCE**

NOTICE AND SIGNATURE PAGE

Using Government drawings, specifications, or other data included in this document for any purpose other than Government procurement does not in any way obligate the U.S. Government. The fact that the Government formulated or supplied the drawings, specifications, or other data does not license the holder or any other person or corporation; or convey any rights or permission to manufacture, use, or sell any patented invention that may relate to them.

This report was cleared for public release by the USAF 88th Air Base Wing (88 ABW) Public Affairs Office (PAO) and is available to the general public, including foreign nationals.

Copies may be obtained from the Defense Technical Information Center (DTIC)
(<http://www.dtic.mil>).

AFRL-RQ-WP-TP-2014-0133 HAS BEEN REVIEWED AND IS APPROVED FOR
PUBLICATION IN ACCORDANCE WITH ASSIGNED DISTRIBUTION STATEMENT.

*//Signature//

TRAVIS E. MICHALAK
Program Manager
Mechanical and Thermal Systems Branch
Power and Control Division

//Signature//

THOMAS L. REITZ, Technical Advisor
Mechanical and Thermal Systems Branch
Power and Control Division
Aerospace Systems Directorate

//Signature//

JOHN G. NAIRUS, Chief Engineer
Power and Control Division
Aerospace Systems Directorate

This report is published in the interest of scientific and technical information exchange, and its publication does not constitute the Government's approval or disapproval of its ideas or findings.

*Disseminated copies will show “//Signature//” stamped or typed above the signature blocks.

REPORT DOCUMENTATION PAGE				<i>Form Approved</i> OMB No. 0704-0188	
The public reporting burden for this collection of information is estimated to average 1 hour per response, including the time for reviewing instructions, searching existing data sources, gathering and maintaining the data needed, and completing and reviewing the collection of information. Send comments regarding this burden estimate or any other aspect of this collection of information, including suggestions for reducing this burden, to Department of Defense, Washington Headquarters Services, Directorate for Information Operations and Reports (0704-0188), 1215 Jefferson Davis Highway, Suite 1204, Arlington, VA 22202-4302. Respondents should be aware that notwithstanding any other provision of law, no person shall be subject to any penalty for failing to comply with a collection of information if it does not display a currently valid OMB control number. PLEASE DO NOT RETURN YOUR FORM TO THE ABOVE ADDRESS.					
1. REPORT DATE (DD-MM-YY) November 2013		2. REPORT TYPE Conference Paper Postprint		3. DATES COVERED (From - To) 01 April 2012 – 08 April 2013	
4. TITLE AND SUBTITLE THIN FILM EVAPORATION MODEL WITH RETARDED VAN DER WAALS INTERACTION (POSTPRINT)				5a. CONTRACT NUMBER In-house	
				5b. GRANT NUMBER	
				5c. PROGRAM ELEMENT NUMBER 62203F	
6. AUTHOR(S) Michael Hanchak, Marlin D. Vangsness, and Jamie S. Ervin (University of Dayton Research Institute) Nadina Gheorghiu (Universal Technology Corporation) Larry Byrd and John G. Jones (AFRL/RQQM)				5d. PROJECT NUMBER 3145	
				5e. TASK NUMBER N/A	
				5f. WORK UNIT NUMBER Q0LA	
7. PERFORMING ORGANIZATION NAME(S) AND ADDRESS(ES) University of Dayton Research Institute 300 College Park Dayton, OH 45469 ----- Universal Technology Corporation Dayton, OH				8. PERFORMING ORGANIZATION REPORT NUMBER AFRL-RQ-WP-TP-2014-0133	
9. SPONSORING/MONITORING AGENCY NAME(S) AND ADDRESS(ES) Air Force Research Laboratory Aerospace Systems Directorate Wright-Patterson Air Force Base, OH 45433-7542 Air Force Materiel Command United States Air Force				10. SPONSORING/MONITORING AGENCY ACRONYM(S) AFRL/RQQM	
				11. SPONSORING/MONITORING AGENCY REPORT NUMBER(S) AFRL-RQ-WP-TP-2014-0133	
12. DISTRIBUTION/AVAILABILITY STATEMENT Approved for public release; distribution unlimited.					
13. SUPPLEMENTARY NOTES PA Case Number: 88ABW-2013-1705; Clearance Date: 08 Apr 2013. The conference paper was presented at the ASME 2013 International Mechanical Engineering Congress and Exposition, held in San Diego, California, from November 15 through 21, 2013 and was published by ASME proceedings of the conference, Paper Number IMECE2013-62397. Note that the word, Interaction, is misspelled in the title of the original published paper but is corrected in the reproduced title of this AFRL cover matter. The U.S. Government is joint author of the work and has the right to use, modify, reproduce, release, perform, display, or disclose the work.					
14. ABSTRACT In phase change heat transfer equipment, three-phase contact regions exist that consist of a solid wall and the liquid and vapor phases of a working fluid. When the working fluid fully wets the solid wall, a microscopic thin film adjoining the meniscus is present called the adsorbed film. Upon heating, a non-uniform evaporative flux profile develops with a maximum value occurring within the transition between the adsorbed film and the intrinsic meniscus. It is important to study the heat transfer characteristics of this region to gain better fundamental understanding and useful design principles. The adsorbed film occurs when the driving potential for evaporation is opposed by the presence of intermolecular forces, represented analytically by the disjoining pressure, which acts to thicken a wetting film. The model presented includes lubrication theory of the liquid flow within the film, heat conduction across the film from the heated wall to the liquid-vapor interface, kinetic theory evaporation from the interface to the vapor phase, and disjoining pressure based on a retarded van der Waals interaction. The retarded van der Waals interaction is derived from Hamaker theory, the summation of retarded pair potentials for all molecules for a given geometry. When combined, the governing equations form a third-order, nonlinear differential equation for the film thickness versus distance, which is solved numerically using iteration of the initial film curvature in order to match the far-field curvature of the meniscus. Also, iteration is required at each length step to determine the liquid-vapor interface temperature. Useful outputs of the model include the liquid-vapor interface temperature and the evaporative mass flux profile. The model is calibrated to in-house experiments that employ an axisymmetric capillary feeder to provide a thin film of n-octane onto a substrate of silicon, where the gas phase is air saturated with vapor. The film thickness versus radial distance is measured using reflectometry and interferometry.					
15. SUBJECT TERMS thin film evaporation, modeling, Retarded Van Der Waals Interaction, heat transfer					
16. SECURITY CLASSIFICATION OF:			17. LIMITATION OF ABSTRACT: SAR	18. NUMBER OF PAGES 16	19a. NAME OF RESPONSIBLE PERSON (Monitor) Travis E. Michalak 19b. TELEPHONE NUMBER (Include Area Code) N/A
a. REPORT Unclassified	b. ABSTRACT Unclassified	c. THIS PAGE Unclassified			

IMECE2013-62397

THIN FILM EVAPORATION MODEL WITH RETARDED VAN DER WAALS INTERACTION

Michael S. Hanchak

University of Dayton Research Institute
Dayton, Ohio, USA

Nadina Gheorghiu

Universal Technology Corporation
Dayton, Ohio, USA

Larry W. Byrd

Air Force Research Laboratory
Wright-Patterson AFB, Ohio, USA

Marlin D. Vangsness

University of Dayton Research Institute
Dayton, Ohio, USA

Jamie S. Ervin

University of Dayton Research Institute
Dayton, Ohio, USA

John G. Jones

Air Force Research Laboratory
Wright-Patterson AFB, Ohio, USA

ABSTRACT

In phase change heat transfer equipment, three-phase contact regions exist that consist of a solid wall and the liquid and vapor phases of a working fluid. When the working fluid fully wets the solid wall, a microscopic thin film adjoining the meniscus is present called the adsorbed film. Upon heating, a non-uniform evaporative flux profile develops with a maximum value occurring within the transition between the adsorbed film and the intrinsic meniscus. It is important to study the heat transfer characteristics of this region to gain better fundamental understanding and useful design principles. The adsorbed film occurs when the driving potential for evaporation is opposed by the presence of intermolecular forces, represented analytically by the disjoining pressure, which acts to thicken a wetting film. The model presented includes lubrication theory of the liquid flow within the film, heat conduction across the film from the heated wall to the liquid-vapor interface, kinetic theory evaporation from the interface to the vapor phase, and disjoining pressure based on a retarded van der Waals interaction. The retarded van der Waals interaction is derived from Hamaker theory, the summation of retarded pair potentials for all molecules for a given geometry. When combined, the governing equations form a third-order, nonlinear differential equation for the film thickness versus distance, which is solved numerically using iteration of the initial film curvature in order to match the far-field curvature of the meniscus. Also, iteration is required at each length step to determine the liquid-vapor interface temperature. Useful outputs of the model include the liquid-vapor interface temperature and the evaporative mass flux profile. The model is calibrated to in-house experiments that employ an axisymmetric capillary feeder to provide a thin film of n-octane onto a substrate of silicon, where the gas phase is air saturated with vapor. The film thickness versus radial distance is measured using reflectometry and interferometry.

INTRODUCTION

Liquid-to-vapor phase change processes can accommodate large heat fluxes, thus they are important in the thermal management of many diverse systems. For example, phase

change heat transfer occurs in the evaporator and condenser of a vapor-compression system and is also important for micro-electronics cooling, spray cooling systems, boiling, and heat pipes. Phase change heat transfer is a more effective vehicle to remove thermal energy than single phase heat transfer given the much larger enthalpy of vaporization compared to the specific heat of the working fluid. Using the latent heat required for phase change can lower the required mass flow rate and inlet and exit temperatures of the working fluid relative to single phase heat exchangers. However, the fundamental mechanisms of heat and mass transport during liquid-to-vapor phase change are poorly understood and remain an active area of research. Particularly important is knowledge of the interfacial phenomena that ultimately determine the large heat transfer rates within evaporators and condensers.

At the contact line present between a wetting liquid and a solid, there exists a thin film region over which large heat fluxes can occur [1, 2]. Since the film is very thin there, the thermal resistance to conduction across it is small, and the liquid-vapor interface temperature is nearly equal to the wall temperature. As the film becomes thinner, it approaches a limit where the intermolecular attraction of the liquid molecules to the surface can negate the tendency of those molecules to evaporate, even at elevated temperatures. This region is called the *adsorbed film*, and it is usually on the order of ten nanometers thick. This region is an important area for study since any detailed physical model of the thin film heat transfer process must include the forces that account for the adsorbed film. As the film thickens to meet the intrinsic meniscus, the forces holding it to the surface weaken and molecules escape through evaporation. However, further thickening of the film will also increase the thermal resistance to conduction and lower the interface temperature. Consequently, there is a point of maximum heat flux where the film is neither too thin for evaporation nor too thick for adequate conduction (see Fig. 1). This entire region is relatively small in terms of area, so it is advantageous to increase the total area or length of the contact line to provide the highest overall heat flux in, say, an evaporator.

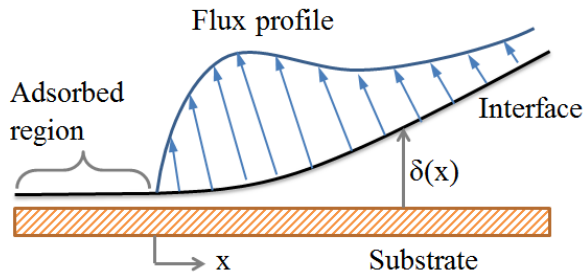


Fig. 1. The thin film region is shown with a typical evaporation profile.

Several researchers have modeled the fluid flow in thin evaporating films, all with varying degrees of simplification of the governing equations [2, 3, 4, 5, 6, 7, 8, 9]. The basic approach is to assume a lubrication analysis of the liquid flow in the thin film and a kinetic-theory based evaporation model from the liquid-vapor interface. These two are linked by the conservation of mass. The temperature at the interface is determined by iterating between 1-D conduction across the liquid film and the evaporative heat flux at the interface, which is the evaporative mass flux multiplied by the enthalpy of vaporization. Once assembled, the theory results in a third-order set of coupled differential equations that require the use of numerical ordinary differential equation (ODE) solvers.

Since the adsorbed film is present due to intermolecular forces, a force versus distance law is assumed. This law can take many forms, from a simple non-retarded disjoining pressure [1,3] to a fully retarded one [9]. These terms are defined in the theory section. The present research incorporates a blended theory proposed by Gregory [10] that correctly predicts both the non-retarded interaction at very thin films and the fully retarded interaction at relatively thicker films.

Below, we describe the experimental setup specially constructed for this research effort. Later we formulate the theoretical model based on both previous work and additional enhancements. Comparison between the empirical data and model simulations will reveal the validity of the model.

EXPERIMENT

Fig. 2 shows a photograph of the thin film test fixture employed to study thin film evaporation. It consists of a base plate, chamber enclosure, and thin film test section. The axisymmetric test section comprises a test surface, for our purposes a silicon wafer, mounted to a wafer holder, over which a capillary feeder plate is bolted. The capillary feeder plate geometry is such that the working side is 0.5 mm above the silicon while the inner chamber is 2.5 mm above the silicon. The capillary feeder top plate is made from aluminum while the base is made from PEEK engineering plastic (Figs. 3 & 4). The parts are aligned by dowel pins and fixed in place by machine screws. The base is then fixed to a bottom plate which serves as the base for the chamber enclosure as well. The device was inspired by the work of [8].

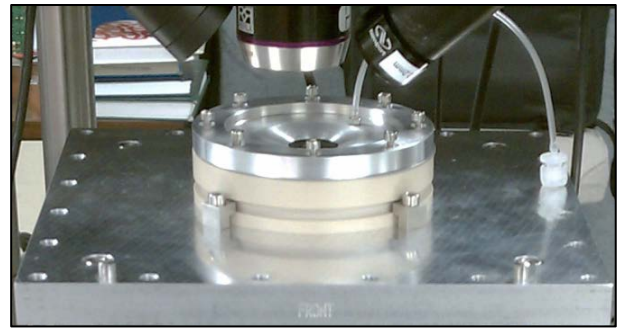


Fig. 2. A Photograph of the capillary test cell. The chamber enclosure is removed for clarity. The reflectometer objective can be seen at the top of the image.

The fixture is enclosed to ensure that the air is saturated with vapor. Only a small port is open to the atmosphere to allow for pressure equalization and bulk vapor transport. Otherwise, the air in the test chamber would become super-saturated and evaporation would cease. Also, the pressure in the chamber would climb as the entire cell became warmer thus allowing a higher vapor partial pressure.

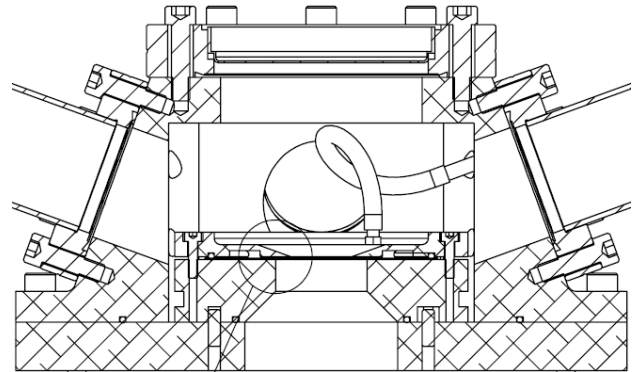


Fig. 3. Cross-section of thin film test fixture with environmental chamber. The central test specimen is axisymmetric around the centerline.

The feeder plate relies on capillary forces to ensure a steady flow of liquid to replenish that lost to evaporation (Fig. 4). The capillary feeder is filled with liquid from a clean syringe until the chamber is mostly filled. As the liquid evaporates from the working side, the liquid interface in the chamber section will recede. As long as the fluid interface in the chamber remains at constant curvature while it travels, the working section will remain steady since the out-of-plane curvature is much smaller than the in-plane. This is slightly different than ref. [8] where a hydrostatic syphon was used to provide a constant flowrate of liquid to the test cell. The downside of using a syphon was the requirement of holding the height of the supply container relative to the height of the test cell constant as the liquid evaporated.

It is important that the backside of the capillary slug be exposed to the same environmental pressure as the working side. This is achieved by a small vent hole (Fig. 4). At equilibrium the bulk menisci curvatures are equal, but deviate near the contact line due to surface forces. The larger gap acts as to supply the small amount of liquid lost to evaporation.

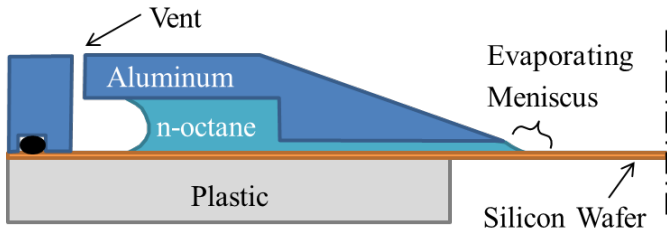


Fig. 4. The capillary feeder geometry.

The substrate is a three inch diameter silicon wafer with a native oxide present that is two to three nanometers thick, verified by ellipsometry. It is cleaned by first rinsing in acetone, then ethanol, and finally allowed to soak in the working fluid overnight. When needed, it is removed from the soaking bath and dried with clean, compressed air and immediately assembled into the test fixture. This is placed inside a HEPA filtered glove box for storage and to prevent contamination.

A circular resistive heater, five Watts maximum, is adhered underneath and centered on the silicon wafer. Heat input can be finely controlled with a power supply. This heat travels radially outward along the silicon wafer. Beneath the transition from adsorbed film to meniscus, which is much less than 1 mm in length, the temperature is basically constant and is measured using thermocouples.

The working fluid is 99+% pure n-octane procured from Sigma-Aldrich. It is transferred from its container to the test area using clean, covered beakers and clean syringes. Cleanliness is paramount as any contamination will result in the contaminant accumulating near the contact line during evaporation of the working fluid. This will create disruptions in the film thickness and evaporation process.

To measure the liquid film thickness, we employ a microscope-based reflectometer (Filmetrics F40-UV). This device analyzes the amplitude of light reflected from the sample across a range of wavelengths from 200 to 1100 nm. The accompanying software can predict the thicknesses of multiple layers based on their optical properties versus wavelength. In the present case, this is silicon/silicon dioxide/n-octane/air. The measurement area of the instrument is $16.7 \mu\text{m}$ square. It has a working distance of approximately 20 mm.

The main limitation of this device is its inability to measure relatively large variations of thickness within its field of view. Thus, to be able to measure film regions with large slopes, we also employ the technique of [8] by imaging the thin film region illuminated with monochromatic light, a 385 nm wavelength light emitting diode (LED), as shown in Fig. 5. Averaging the pixel intensity in the vertical direction produces a sinusoidal grayscale intensity versus horizontal distance (Fig. 6(a)). By applying the theory of multiple reflections from three planar media, as detailed in [9], the film thickness can be calculated from the scaled intensity plot (Fig. 6(b)). For example, the first dark fringe occurs at $\lambda/4n_f = 385/(4 \cdot 1.398) = 69 \text{ nm}$. Below around one-eighth wavelength of the incident light, the uncertainty in the intensity is too great to give an accurate thickness. Since the transfer function from intensity to thickness has an inverse

cosine term, which is multi-valued, the order of the oscillation must be counted to apply the proper angular phase shift.

The test fixture is mounted on a Zaber micro-positioning motorized stage to move it horizontally underneath the reflectometer. The stage is set in motion at a prescribed velocity while the reflectometer takes continuous measurements with time stamps. When the speed of the stage is compared to the reflectometer sample times, the film profile versus distance is easily calculated.

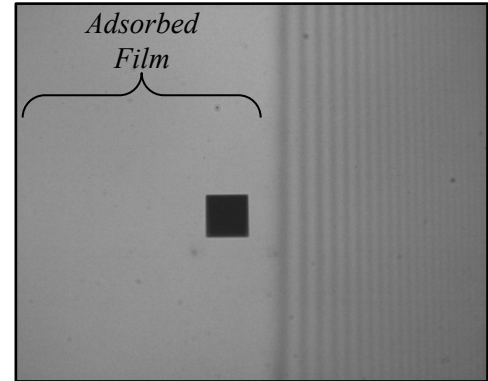
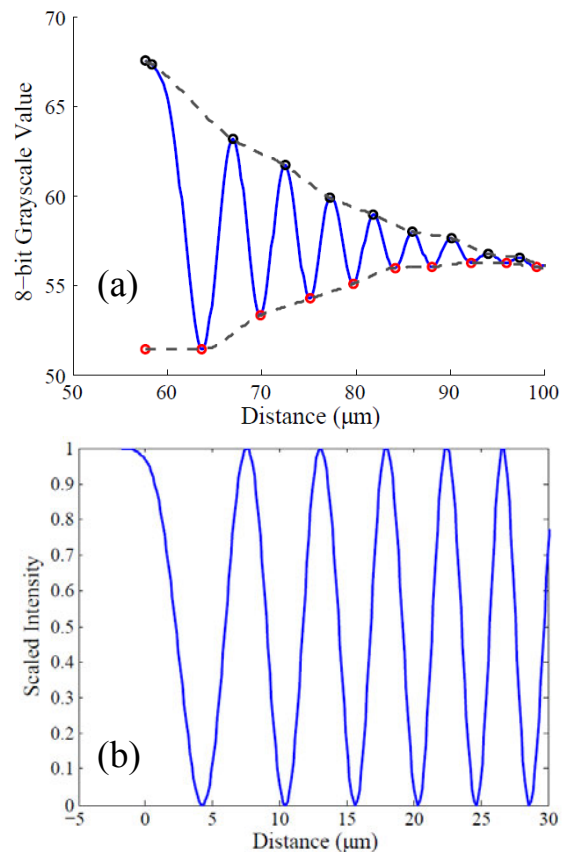


Fig. 5. Micro-photograph of interference fringes of a thin film of n-octane on silicon. The illumination originates from a 385 nm UV LED. The film thickens from left to right. The black square is the measurement area of the reflectometer.



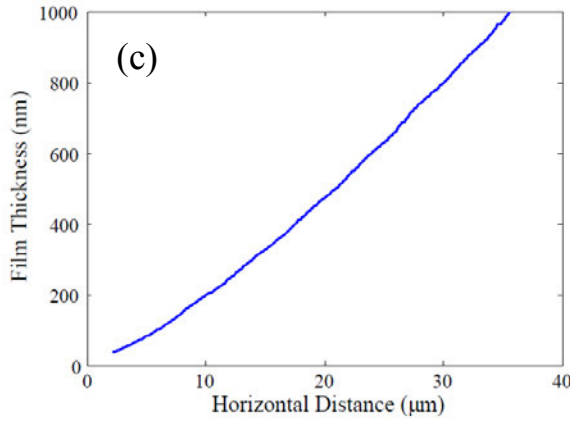


Fig. 6. Process of calculating the film profile from optical interference patterns using an optical transfer function: (a) raw averaged 8-bit grayscale versus distance; (b) scaled intensity using upper and lower bounding curves; (c) resulting thickness profile.

THEORY

When surfaces approach each other within very small distances, intermolecular forces will have a significant effect on the behavior of bulk systems, such as colloidal dispersions and thin films. This section provides a brief explanation of these forces and their macroscopic ramifications. Further details can be found in [11] and [12].

The electrostatic attractive force between any two molecules is very short range (< 5 nm). However, the summation of all interactions between all molecules within condensed phases can generate very large and much longer range forces (beyond 50 nm). These forces are electrostatic in nature and arise from the attraction between both permanent and induced dipoles in the molecules. The interaction energies, or *pair potentials*, of most importance are a function of the inverse sixth power of distance; these are collectively known as the van der Waals interactions [11]. The interaction force is the negative derivative with respect to distance of the interaction energy. The method due to Hamaker essentially sums all pair potentials between individual atoms or molecules to obtain the total interaction between condensed phases [11].

The macroscopic manifestation of the van der Waals forces between two planar surfaces is called the *disjoining pressure* [1, 11]. When applied to systems of two phases acting across a medium, the disjoining pressure can either be positive or negative. For the silicon/n-octane/air system under consideration, the liquid pressure is lowered, which draws liquid from a region of higher pressure, say a reservoir or meniscus, to thicken the thin film. Hence, octane is said to fully wet silicon. In contrast, a non-wetting thin film becomes thinner until it ruptures to produce discrete droplets on the substrate. The net attractive force between the solid substrate and the liquid behave as though a repulsive force (negative pressure) exists between the gas/liquid surface and the solid surface. The non-retarded disjoining pressure between two planar surfaces separated by δ is given by

$$P_{d,non-ret} = \frac{A_{non-ret}}{6\pi\delta^3}, \quad (1)$$

where A is called the Hamaker constant or Hamaker coefficient. It is a function of the atomic densities of the constituents and the strength of the pair potential between them. By measuring the forces between macroscopic objects, such as with a surface force apparatus, the Hamaker coefficient can be determined [11]. The Hamaker coefficient for a wetting film is negative.

This additivity approach assumes superposition of all interaction potentials. However, real materials behave such that the polarizability of atoms, which cause induced dipoles, is affected by neighboring atoms. Thus, instead of the method of Hamaker, the macroscopic forces between condensed phases can be elucidated using Lifshitz theory. This method utilizes quantum field theory and requires knowledge of the dielectric constants and refractive indices of the bulk phases, as well as their frequency dependences (through dispersion relations). On the whole, this theory is complicated but simplifications have been provided [11]. Using this theory, we determine the non-retarded Hamaker constant for the silicon/n-octane/air system to be -1.464×10^{-19} J.

Another complication that arises is the retardation of the intermolecular forces at larger separations. Retardation, or diminishing of the force, occurs because of the finite travel time of the interaction. Over time, the instantaneous dipoles of the molecules rotate a finite amount, leading to a diminished attractive force [11]. At large separations, the disjoining pressure behaves as the inverse fourth power of distance, namely

$$P_{d,ret} = \frac{B_{ret}}{\delta^4}, \quad (2)$$

This expression requires the determination of a new force coefficient and is only valid beyond a certain distance.

Gregory [10] provides a model of the disjoining pressure based on the semi-empirical work of Overbeek [13]. Overbeek's model used the Hamaker approach of additivity with a pair potential that incorporates the effect of retardation. Gregory's analysis results in a compact expression that includes non-retarded and retard terms,

$$P_d = \frac{A_{non-ret}}{6\pi\delta^3} \frac{(1+3b\delta/2\lambda)}{(1+b\delta/\lambda)^2}, \quad (3)$$

where b is an empirical factor equal to 5.32 and λ is a characteristic wavelength equal to 100 nm. In the limit of small and large separation distances, the Gregory theory replicates both the inverse third power (1) and inverse fourth power (2) dependencies of distance, respectively (Fig. 7). Previously, Truong and Wayner used Dzyaloshinskii-Lifshitz-Pitaevskii theory to calculate the force between planar surfaces. They presented a table of Hamaker "constants" versus distance [14]. Again, the Hamaker constant is not truly constant due to the effects described above. The advantage of the theory by Gregory is that it does not require tabulated values of the Hamaker coefficient versus distance.

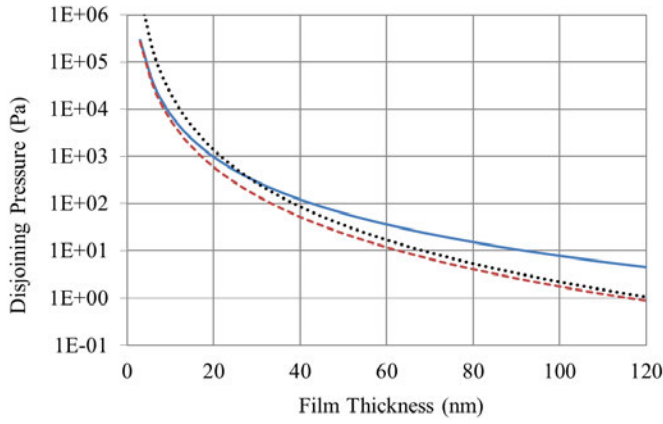


Fig. 7. Comparison of disjoining pressure for three theories: inverse third power (solid), inverse fourth power (dotted), and the blended theory of Gregory (dashed).

Fluidic Model

The fluid flow in the thin film is assumed to behave according to steady-state lubrication theory, where time is ignored and the inertial forces are very small in comparison to the pressure and viscous forces. Also, variations of velocity in the y direction are ignored and the film height is the dependent variable along the horizontal distance. What follows is similar to the analysis of [6].

The governing equation of fluid flow reduces to

$$\frac{\partial P_l}{\partial x} = \mu \frac{\partial^2 u}{\partial y^2} \quad (4)$$

A parabolic velocity profile in the film is assumed, given by $u(x, y) = U(x) \left(2 \frac{y}{\delta} - \left(\frac{y}{\delta} \right)^2 \right)$, where $U(x)$ is the velocity at the surface of height δ ; no-slip was imposed at the substrate. Hence, (4) becomes

$$\frac{\partial P_l}{\partial x} = -2\mu \frac{U(x)}{\delta^2} \quad (5)$$

Integrating the velocity profile times the density and using (5) to eliminate $U(x)$ gives the flowrate per unit width in the film versus x ,

$$\Gamma(x) = -\frac{1}{3\nu} \delta^3 \frac{dP_l}{dx} \quad (6)$$

Thus, for an imposed pressure field, we can calculate the flowrate within the film. The difference in flowrate from one point to another an infinitesimal distance away must equal the mass flux lost to evaporation at the surface, namely

$$-m'' = \frac{d\Gamma(x)}{dx} = \frac{d}{dx} \left(-\frac{\delta^3}{3\nu} \frac{dP_l}{dx} \right) \quad (7)$$

The evaporation is calculated using kinetic theory, more specifically, by the model due to Schrage [15]. This model is applicable for a planar interface evaporating into an environment of its own vapor where the partial pressures of vapor are known:

$$m'' = \frac{2\sigma}{2-\sigma} \sqrt{\frac{\mathcal{M}}{2\pi\mathcal{R}}} \left(\frac{P_{lv}}{\sqrt{T_{lv}}} - \frac{P_v}{\sqrt{T_v}} \right) \quad (8)$$

Here, \mathcal{M} is the molecular mass of the fluid, \mathcal{R} the universal gas constant, P_{lv} is the vapor pressure at the interface and P_v is the vapor partial pressure in the gas phase adjacent to the interface, both assumed to be saturated at their respective temperatures, T_{lv} and T_v . The gas phase is a perfect mixture of vapor and air. The accommodation coefficient is denoted by σ and represents the fraction of molecules which are released from the interface from those that emerge from the interface [16]. Here, σ is taken to be unity.

In an open system, the partial pressure of vapor near the interface would be unknown and would require additional equations describing the diffusion and advection of vapor into the atmosphere. However, with the interface assumed to be saturated at the interface temperature and the vapor in the gas phase saturated at a slightly lower temperature, the potential that drives evaporation is known if the temperatures are known.

The conduction across the film is approximated as being equal to the evaporative heat flux,

$$m'' h_{fg} \cong k_l \frac{(T_w - T_{lv})}{\delta}, \quad (9)$$

where k_l is the film thermal conductivity, h_{fg} is the enthalpy of vaporization, and T_w and T_{lv} are the wall and interface temperatures, respectively. This equation has no closed form solution for the interface temperature given the dependency of the mass flux on temperature and vapor pressure. This approximation is valid given the Péclet number, for this case $Pe = Re \times Pr = 0.004 \ll 1$. Thus, the thermal capacity of the fluid moving through the film is much less than the conduction across it.

As temperature and total pressure change, so does the partial pressure of saturated vapor. The saturation pressure of vapor at the interface can be depressed by the presence of a pressure drop across the interface due to curvature and disjoining pressure. The equations that govern this process are developed from the thermodynamics of phase equilibrium. Specifically, the variation in vapor pressure p_v , a measure of escaping tendency, to total pressure is governed by

$$\left. \frac{d(\ln p_v)}{dP} \right|_T = \frac{v_l}{RT}, \quad (10)$$

Where v is the specific volume of the liquid, R is the specific gas constant, and T is the absolute temperature [17]. This equation can be integrated from the case of a flat, bulk liquid-vapor interface to the case of a curved, thin-film interface near a solid surface, the LHS being vapor and the RHS being liquid. Upon integrating, we achieve

$$P_{lv, equ}(T_{lv}) = P_{sat}(T_{lv}) \exp \left\{ \frac{P_{lv, equ}(T_{lv}) - P_{sat}(T_{lv}) + P_d + P_c}{\rho_l R T} \right\}, \quad (11)$$

which describes the variation of vapor pressure due to mechanical pressure differences in the liquid. Here, $P_{lv, equ}$ is the actual equilibrium vapor pressure at the interface, P_{sat} is the normal saturation pressure at the interface temperature, and P_d and P_c are the disjoining and capillary pressures, respectively. This equation was previously stated by [1, 6, 18] and has been called the Deryagin-Zorin equation, the modified Kelvin equation, and the Gibbs equation. It is the vapor pressure predicted by this equation that is used in the kinetic

evaporative flux equation as the vapor pressure at the liquid-vapor interface.

Likewise, the variation in vapor pressure due to temperature is governed by the equilibrium equation

$$\left. \frac{d(\ln p_v)}{dT} \right|_P = \frac{h_{fg}}{RT^2}. \quad (12)$$

Upon integration along the saturation curve, this gives the familiar Clausius-Clapeyron relation, which describes the change in saturation pressure with temperature, i.e.

$$P_{sat}(T) = P_{sat}(T_{ref}) \exp \left\{ \frac{h_{fg}}{R} \left(\frac{1}{T_{ref}} - \frac{1}{T} \right) \right\}. \quad (13)$$

To link the system of equations, we write the pressure balance across the liquid-vapor interface as

$$P_l = P_v + P_d + P_c. \quad (14)$$

The capillary pressure due to curvature and surface tension, γ , is given by the familiar Young-Laplace equation,

$$P_c = \gamma \left(\frac{1}{R_1} + \frac{1}{R_2} \right) \approx -\gamma \frac{\delta''}{(1+\delta'^2)^{3/2}} \quad (15)$$

The negative sign in this equation reflects the fact that a concave liquid interface with positive curvature actually reduces the liquid pressure. Also, the second radius of curvature (out-of-plane) is much larger than the meniscus radius and is ignored.

Combining equations (3), (7), (14) and (15) and defining $\bar{A} = A/6\pi$ produces the governing differential equation of interface height versus distance,

$$-m'' = \frac{d}{dx} \left[\frac{\delta^3}{3\nu} \left(\frac{\gamma \delta'''}{(1+\delta'^2)^{3/2}} - \frac{3\gamma \delta' \delta''^2}{(1+\delta'^2)^{5/2}} - \frac{\bar{A} \lambda \delta' (3\lambda^2 + 8b\lambda\delta + 6b^2\delta^2)}{\delta^4 (\lambda + b\delta)^3} \right) \right]. \quad (16)$$

To review, heat drives the substrate temperature which, through conduction, drives the interface temperature. The increase in interfacial temperature relative to the vapor phase provides the potential difference for evaporation. Evaporative heat flux and conduction must equilibrate to determine the ultimate interface temperature. Finally, the loss of fluid due to evaporation is replenished by bulk liquid flow driven by pressure gradients, which depend on and influence the liquid interface shape. In regions of high disjoining pressure, evaporation will be suppressed. As the film thickens, first the disjoining pressure drops and evaporation is enhanced; then the interface temperature drops and evaporation is lessened. Thus, there is a region of maximum evaporation.

Numerical Method

The temperature difference between the wall and the gas phase is found using the method of [6]. In the adsorbed film region, there is no evaporation and the liquid interface is assumed to be at the same temperature as the substrate. Also, there is zero curvature there. Hence, with $T_w = T_v$ and $m'' = 0$, (8) and (11) can be combined into

$$\rho_l R T_w \ln \left(\frac{P_v}{P_{sat}(T_w)} \sqrt{\frac{T_w}{T_v}} \right) - P_v \sqrt{\frac{T_w}{T_v}} + P_{sat}(T_w) = P_{d,0}. \quad (17)$$

A zero-finding algorithm is then used to find T_w given the measured adsorbed film thickness. If the substrate temperature is accurately known, the gas temperature adjacent to the interface is found by instead solving (17) for T_v . In practice, the temperature difference between the wall and the vapor is a fraction of a degree Kelvin. Both the wall temperature and vapor temperature are assumed constant along the x direction; the interface temperature at any distance falls between these two values and depends on the heat flux. Alternatively, the required dT to offset the disjoining pressure in the adsorbed film can be obtained by setting the total derivative of vapor pressure to zero (comprised of (10) and (12) multiplied by dP and dT , respectively, then added). While this method ignores the zero mass flux condition of (8), it provides the correct dT within 3% of (17).

When implementing the governing equations numerically, one must provide boundary conditions at the beginning of the numerical integration, which then proceeds lengthwise using a specified increment, dx . The thickness boundary condition was set to 2% larger than the measured adsorbed film thickness to ensure a non-zero mass flux and prevent a trivial, flat profile. The profile first derivative (slope) was set to zero. As the film becomes thicker, its curvature must approach the intrinsic meniscus curvature. Thus the initial curvature must be chosen to produce the desired final curvature. This is a shooting problem, where an initial condition must be iteratively determined to satisfy a far-field condition. The proper initial curvature was determined using the bisection algorithm. MATLAB [19] was used as the programming language given its rich feature set of numerical routines, graphics capabilities, and ease of implementation.

To simplify execution, the argument of the derivative of (16) is replaced by β , namely

$$\beta = \frac{\delta^3}{3\nu} \left(\frac{\gamma \delta'''}{(1+\delta'^2)^{3/2}} - \frac{3\gamma \delta' \delta''^2}{(1+\delta'^2)^{5/2}} - \frac{\bar{A} \lambda \delta' (3\lambda^2 + 8b\lambda\delta + 6b^2\delta^2)}{\delta^4 (\lambda + b\delta)^3} \right). \quad (18)$$

The ODE solver requires that the governing equation (16) be recast in vector form. Taking state variables as $\{y_1; y_2; y_3; y_4\} = \{\delta; \delta'; \delta''; \beta\}$, their derivatives are given by

$$\begin{Bmatrix} y_1' \\ y_2' \\ y_3' \\ y_4' \end{Bmatrix} = \begin{Bmatrix} \delta' \\ \delta'' \\ \delta''' \\ \beta' \end{Bmatrix} = \begin{Bmatrix} y_2 \\ y_3 \\ \frac{3y_2 y_3^2}{1+y_2^2} + \frac{(1+y_2^2)^{3/2}}{\gamma y_1^2} \left(3\nu y_4 + \bar{A} \lambda \frac{y_2 (3\lambda^2 + 8b\lambda y_1 + 6b^2 y_1^2)}{(\lambda + b y_1)^3} \right) \\ -m'' \end{Bmatrix}. \quad (19)$$

The third element of this vector was obtained by solving (18) for δ''' . This derivative vector was coded into a separate file and called by the ODE solver at every horizontal distance step.

The interface temperature required to calculate the mass flux in (19) is not known. However, the evaporative heat flux at any point on the interface must equal the film conduction there, and both are dependent on the interface temperature. Therefore, we used a relaxation scheme to iterate the interface temperature between equations (8) and (9) until they agreed within a prescribed tolerance (10^{-5}). This was done at every

distance step before the calculation of (19). Once (19) was determined, the ODE solver could integrate the state vector and move to the next distance step.

RESULTS

To illustrate measurement repeatability, Fig. 8 shows multiple reflectometer scans for the same thin film profile taken within one hour. A Gaussian smoothing filter was applied to eliminate high frequency noise. At the far left, the film is adsorbed with a thickness around 13 nm. While the reflectometer reported values of thickness beyond 25 nm, these values are uncertain since the goodness of fit reported by the software fell off quickly due to the increasing slope present. Thus, the reflectometer data was truncated at film thicknesses of 25 nm for comparison to the model. Nevertheless, flat films of several micrometers in thickness are accurately measured. Also, the interferometry data was truncated below one eighth wavelength of the monochromatic light source, or about 40 nm. Thus, there is a gap between the two measurement methods, one which we shall endeavor to bridge in future work.

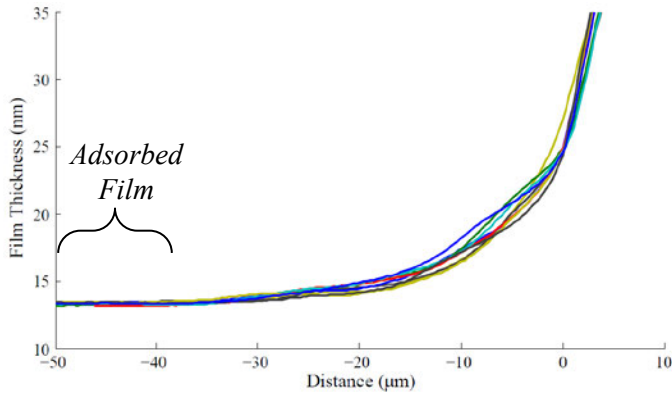


Fig. 8. Reflectometer repeatability results: ten scans of the same film over one hour.

Since the measurement gap exists, the techniques are joined by noting the relative movement of the translation stage to the position of the first dark fringe, whose thickness is well understood. We did, however, notice some backlash in the translation stage stepper motor. Therefore, several micrometers of relative error are expected when aligning the two methods. This discrepancy is expected to vanish once we are successful measuring between 25 and 40 nm and may be accomplished by decreasing the reflectometer measurement area by either 1) installing a smaller aperture in the instrument or 2) increasing the objective lens magnification. The current aperture is 250 μm and the objective magnification is 15 \times . Thus, the measurement area is $250/15 = 16.7 \mu\text{m}$. In terms of interferometry, the 385 nm wavelength source was the shortest wavelength LED available with the power to adequately illuminate the entire field.

For a non-heated substrate, evaporation occurs when the chamber that encloses the test section is vented to the atmosphere. However, near the liquid interface, the gas is still saturated with vapor and the model derived above is valid. Fig. 9 shows the model prediction of the interface shape against the measured data from the reflectometer and the interference fringes. The value at $-10 \mu\text{m}$ corresponds to the adsorbed film. Fig. 10 is the same plot but at a different level

of magnification. The model fits the experimental data quite well. Once the adsorbed film thickness was entered, the model determined the proper wall temperature by solving (17) and then integrated the ODE vector. Again, iteration of the initial film curvature was needed to match the far field curvature of the experimental data, which was 480 m^{-1} for the present case.

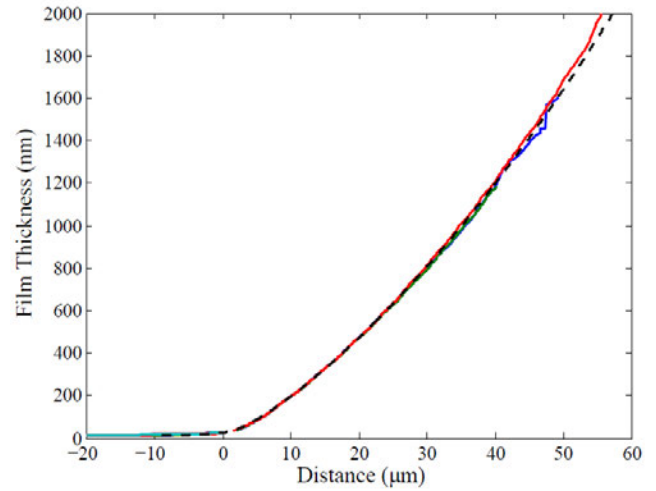


Fig. 9. Model simulation (dashed line) versus both reflectometer and interferometry data is given.

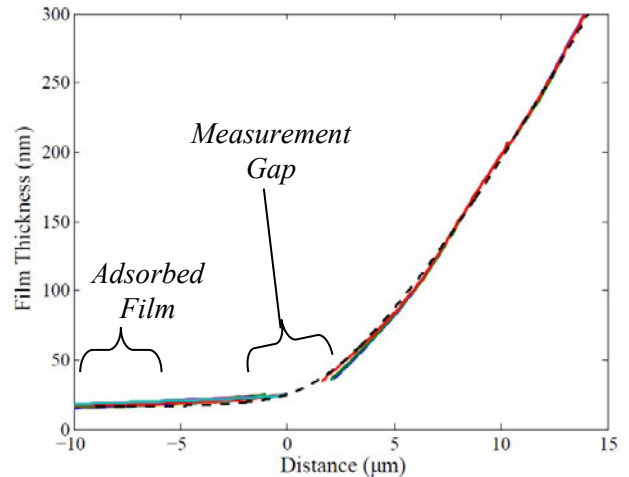


Fig. 10. Enlargement of Fig. 9. Model simulation is dashed line.

For comparison, Fig. 11 illustrates the output of the WGM model [6] both as published and also augmented with the new disjoining pressure formula, eq. (3). The flux profiles are significantly different because the non-retarded disjoining pressure is greater in magnitude than the retarded one, and requires a greater ΔT to suppress evaporation for the same adsorbed film thickness. Hence the wall temperatures for the two disjoining pressure expressions are different in the figure. The overall mass flux is greater with a larger wall temperature. Thus, the choice of the disjoining pressure expression has a significant effect on the mass and heat transfer simulation.

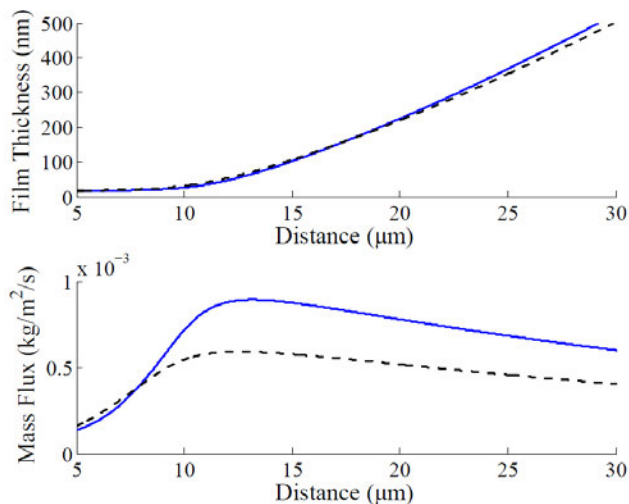


Fig. 11. A comparison of both film profile and evaporative mass flux versus horizontal distance for non-retarded (solid) and retarded (dashed) disjoining pressure.

Fig. 12 illustrates both the evaporative flux profile and the film curvature as a function of distance for the new model. For this particular simulation, the maximum flux occurred at a distance of 12.6 μm from the adsorbed film region, the film being 62 nm thick. For comparison, the adsorbed film was 16 nm thick. Also, the maximum curvature was 10.3 μm from the adsorbed region at a film thickness of 34 nm. The maximum flux occurs where eq. (18) goes through an inflection point.

This figure emphasizes how the evaporative mass flux rises sharply to a maximum, then falls off slowly. Near the maximum flux there is competition between the disjoining pressure due to thinness, the capillary pressure due to curvature, and the loss of interface temperature due to conduction. The balance of these interactions ultimately determines the interface shape.

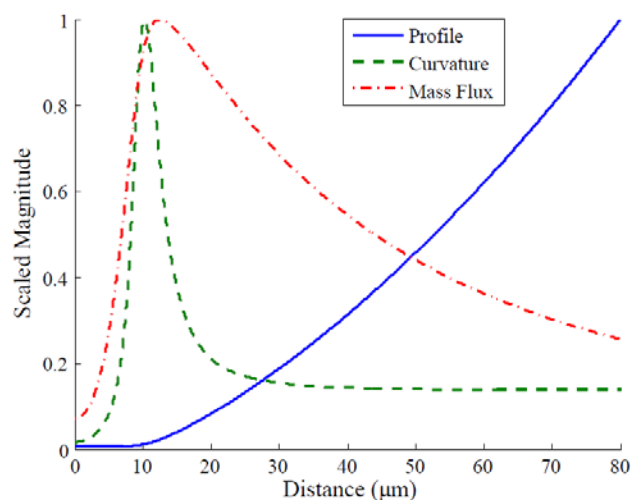


Fig. 12. Film profile, curvature, and mass flux contours scaled to their respective maxima versus distance. In this instance, the maximum mass flux occurred 12.6 μm from the adsorbed region at a film thickness of 62 nm.

Earlier, we determined the small temperature difference between the solid surface and the vapor. Given the strong dependency of vapor pressure on temperature, this small dT was enough to balance the intermolecular forces in the adsorbed film region, thus preventing evaporation there. Fig. 13 shows a plot of the interface temperature versus distance predicted by the model. Note how the interface temperature (solid line) lies between the wall and vapor temperatures (indicated by dashed lines), which obeys our assumption of simple conduction across the thin film. Again, the interface temperature is determined by film resistance and heat conduction, which must equal the evaporative heat flux.

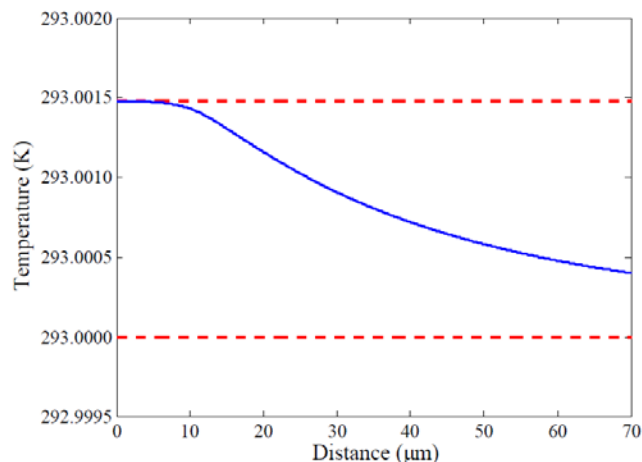


Fig. 13. Temperature profile of thin film liquid/gas interface is shown. The adsorbed film starts at the left side, where the interface temperature is assumed to equal the wall temperature.

CONCLUSION

A numerical model of thin film evaporation was presented that included a retarded van der Waals interaction. This force was represented by the disjoining pressure, which is necessary for the formation of an adsorbed film where evaporation is suppressed.

An experimental fixture was created to study thin film evaporation at different temperatures. Reflectometry and interferometry provided the thin film profile versus horizontal distance. Comparisons were made between the theoretical simulations and the empirical data. The model was then used to infer the evaporative flux profile and point of greatest evaporation.

Several points are emphasized:

- 1) The expression of ref. [10] for the disjoining pressure provided an easy and compact way of capturing both non-retarded and retarded intermolecular interactions across the entire film thickness range.
- 2) The evaporative flux is mediated by the conduction between the heated wall and the interface due to the coupled nature of the mass and energy equations.
- 3) The reflectometer provided a convenient means of determining the film profile for thicknesses where interferometry was not possible.

Future work will explore the impact of varying the accommodation coefficient and quantifying its effect on

theoretical film profiles. Multiple substrate temperatures will be studied by measuring film profiles at different applied heater powers. Also, changes to the instrumentation are required to provide experimental thickness data in the range of 25 to 40 nm.

Finally, our group intends to measure disjoining pressure versus film thickness for a variety of alkanes on silicon and metalized silicon substrates. This will provide empirical values of $A_{non-ret}$, λ , and b in (3), rather than solely relying on theoretical calculations.

ACKNOWLEDGEMENT

This material is based on research sponsored by U.S. Air Force Office of Scientific Research under Grant No. 3002AR5P. The views and conclusions contained herein are those of the authors and should not be interpreted as necessarily representing the official policies or endorsements, either expressed or implied, of U.S. Air Force Office of Scientific Research or the U.S. Government.

We would like to thank Victor Tsao (UDRI) for his technical support.

NOMENCLATURE

A	Hamaker coefficient	δ	film thickness
b	Gregory constant	γ	surface tension
h_{fg}	enthalpy of vap.	λ	Gregory constant
k	thermal conductivity	μ	absolute viscosity
m''	evap. mass flux	ν	kinematic viscosity
M	molecular mass	ρ	density
p	vapor pressure	σ	accom. coefficient
P	pressure	Γ	mass flow per width
R	specific gas constant		
\mathcal{R}	universal gas constant	<i>subscripts</i>	
q''	heat flux	0	adsorbed region
T	temperature	c	capillary
u	fluid velocity	d	disjoining
U	surface velocity	l	liquid
v	specific volume	lv	liquid-vapor
x	horizontal coordinate	v	vapor
y	vertical coordinate	w	wall
		<i>superscripts</i>	
		$''$	per unit time & area
		$'$	derivative w.r.t. x

REFERENCES

- [1] Carey, V.P., Liquid-Vapor Phase-Change Phenomena, Hemisphere Publ. Corp., (1992)
- [2] Potash M. & Wayner P.C. Jr., Evaporation from a Two-Dimensional Extended Meniscus, Int. J. Heat Mass Transfer, 15 (1972) 1851-1863
- [3] DasGupta S., Schonberg J.A., & Wayner P.C. Jr., Investigation of an Evaporating Extended Meniscus Base on the Augmented Young-Laplace Equation, ASME J. Heat Transfer, 115 (1993) 201-208
- [4] Wayner P.C., Jr., Kao Y.K., & LaCroix L.V., The Interline Heat-Transfer Coefficient of an Evaporating Wetting Film, Int. J. Heat Mass Transfer, 19 (1976) 487-492
- [5] Hallinan K.P. & Chebaro H.C., Evaporation from an Extended Meniscus for Nonisothermal Interfacial Conditions, J. Thermophysics & Heat Transfer, 8 (1994) 709-716
- [6] Wang H., Garimella, S.V., & Murthy J.Y., Characteristics of an evaporating thin film in a microchannel, Int. J. Heat Mass Transfer, 50 (2007) 3933-3942
- [7] Wayner Jr., P.C., The effect of interfacial mass transport on flow in thin liquid films, Colloids and Surfaces, 52 (1991) 78-84
- [8] Wayner, P.C., DasGupta, S. and Schonberg, J., Effect of Interfacial Forces on Evaporative Heat Transfer in a Meniscus, Air Force Technical Report WL-TR-91-2061 (1991)
- [9] Sujanani, M. and Wayner Jr., P. C., Microcomputer-Enhanced Optical Investigation of Transport Processes with Phase Change in Near-Equilibrium Thin Liquid Films, Journal of Colloid and Interface Science, 143 (2) (1991)
- [10] Gregory J., Approximate Expressions for Retarded van der Waals Interaction, J. Colloid & Interface Sci., 83 (1981) 138-145
- [11] Israelachvili, J., Intermolecular and Surface Forces, 2nd Edition, Academic Press, London (1992)
- [12] Hiemenz, P. C. and Rajagopalan, R., Principles of Colloid and Surface Chemistry, 3rd Edition, Marcel Dekker, NY (1997)
- [13] Overbeek, J. Th. G., in Colloid Science (H. R. Kruyt, Ed.), Elsevier, Amsterdam, 1 (1952) 266
- [14] Truong, J. G. and Wayner Jr., P. C., Effects of capillary and van der Waals dispersion forces on the equilibrium profile of a wetting liquid: Theory and experiment, J. Chem. Phys. 87, (7) (1987)
- [15] Schrage, R. W., A Theoretical Study of Interphase Mass Transfer. Columbia Univ. Press, New York (1953)
- [16] M. Bond and H. Struchtrup, Mean evaporation and condensation coefficients based on energy dependent condensation probability, Physical Review E 70, 061605 (2004)
- [17] Denbigh, K., The Principles of Chemical Equilibrium, 3rd edition, Cambridge Univ. Press (1971)
- [18] Faghri, A. and Khrustalev, D., Micro/Miniature Heat Pipe Analysis, Air Force Technical Report WL-TR-94-2085 (1994)
- [19] MATLAB r2010a, The MathWorks, Natick, MA